



SPE 109547

Experimental Validation of Pore-Level Calculations of Static and Dynamic Petrophysical Properties of Clastic Rocks

G. Jin, SPE, The University of Texas at Austin; **C. Torres-Verdín**, SPE, The University of Texas at Austin; **F. Radaelli**, ENI Exploration and Production; and **E. Rossi**, ENI Exploration and Production

Copyright 2007, Society of Petroleum Engineers

This paper was prepared for presentation at the 2007 SPE Annual Technical Conference and Exhibition held in Anaheim, California, U.S.A., 11-14 November 2007.

This paper was selected for presentation by an SPE Program Committee following review of information contained in an abstract submitted by the author(s). Contents of the paper, as presented, have not been reviewed by the Society of Petroleum Engineers and are subject to correction by the author(s). The material, as presented, does not necessarily reflect any position of the Society of Petroleum Engineers, its officers, or members. Papers presented at SPE meetings are subject to publication review by Editorial Committees of the Society of Petroleum Engineers. Electronic reproduction, distribution, or storage of any part of this paper for commercial purposes without the written consent of the Society of Petroleum Engineers is prohibited. Permission to reproduce in print is restricted to an abstract of not more than 300 words; illustrations may not be copied. The abstract must contain conspicuous acknowledgment of where and by whom the paper was presented. Write Librarian, SPE, P.O. Box 833836, Richardson, Texas 75083-3836 U.S.A., fax 01-972-952-9435.

Abstract

We present an integrated approach to calculate fundamental macroscopic static and dynamic properties of porous media, including absolute permeability, formation factor, relative permeability, capillary pressure, and resistivity index. The calculations are based on high-resolution three-dimensional (3D) digital images of actual clastic rocks acquired with X-ray computed tomography (CT). Pore-level simulations of single-phase fluid flow and electrical conduction are performed using the lattice-Boltzmann method and diffusion random walks, respectively. Two-phase immiscible fluids are geometrically distributed into the pore space of the synthetic rock using a simple percolation algorithm while enforcing capillary equilibrium. These simulations serve to calculate effective medium properties of macroscopic rock behavior that can be used to improve both the interpretation of well-log measurements and the prediction of multiphase flow properties.

To test and validate our pore-scale model, we consider three micro-CT images of quartzose sandstones with different petrophysical properties to perform both laboratory

measurements and pore-level calculations. The calculated permeability is in good agreement with the corresponding laboratory measurements for clean sands, while it differs for the shaly-sand sample. For both cases, the computed formation factor is consistent with laboratory measurements. For the case of two-phase simulations of water-wet conditions, the derived capillary pressure, relative permeability and resistivity index closely agree with experimental measurements when immovable fluid saturations of oil and water are taken into account. Our simulations show that calculations performed on a small rock sample may not always be representative of heterogeneous rock formations. We also find that the amount of clay-bound water should be accounted for in pore-level petrophysical studies, especially for rocks containing a significant amount of clay minerals. Higher image resolution than available is needed to accurately quantify macroscopic petrophysical properties of such complex rock samples.

Introduction

The quantitative prediction of continuum flow descriptors of porous media, such as absolute permeability, relative permeability, capillary pressure, formation resistivity, *etc.*, is essential in earth sciences and – in particular – petroleum engineering. Usually, the theoretical prediction of rock petrophysical properties is performed in two steps: (1) A model of the rock's microstructure is formulated, and (2) a discretized field equation, such as Stokes' or Laplace's equation, is numerically solved in the context of this model.¹

Predicting rock flow properties requires an accurate 3D spatial representation of the rock microstructure. In the past decades, several methods have been proposed to reconstruct the microstructure of a natural porous medium, such as experimental,²⁻⁶ statistical,⁷⁻¹² process-based,¹³⁻¹⁷ and geometrical¹⁸⁻²⁰ methods, to name just a

few. Numerical techniques have been instructive to understand the general properties of porous media, and particularly useful when experiments are difficult or expensive, as in the cases of core materials not suited for laboratory testing, including drill cuttings, sidewall cores, or damaged cores. Another merit of numerical simulation methods is that they allow the possibility of calculating in a relatively short period of time numerous what-if scenarios, or to conduct sensitivity studies, such as the effect of grain sizes, clay minerals, or saturation history on flow properties of porous media. As predictive as these numerical techniques may be, it is also desirable to directly measure the microstructure experimentally, so as to test and validate the numerical simulations.

Direct measurements of microstructure of porous media are now readily available from X-ray computed microtomography^{2,4,5} and laser confocal microscopy.³ These techniques provide the opportunity to experimentally obtain 3D pore-level images of sedimentary rocks with a spatial resolution of the order of micrometers. One can then perform numerical calculations of petrophysical properties directly on the measured 3D micro-CT images.²¹⁻²³ More importantly, these techniques are non-intrusive, thereby leaving the sample intact and unaltered, allowing complementary studies through direct experimental measurement of petrophysical properties on the same sample. This desirable solution provides benchmark results (micro-CT images and laboratory measurements) against which to test numerical approaches to reconstruct the microstructure of porous materials or numerical methods to calculate petrophysical properties on the digital images.

While pore-level petrophysical studies shed considerable light to macroscopic properties of rocks, significant work remains to validate these studies with laboratory measurements. Usually, Fontainebleau sandstone was used as the ideal experimental system to test and validate pore-level numerical studies because a considerable number of experimental 3D micro-CT images and measured transport properties are available for that system.²²⁻²⁴ However, Fontainebleau sandstone is highly homogenous, consisting of a single mineral (quartz), does not contain clay, and only displays intergranular porosity.²³ In addition, it is imperative to further investigate the effect of image resolution, finite sample size, and distribution of irreducible wetting-phase saturation on the calculation of transport properties from digital images of complex rocks, such as shaly sands. The assumption of a digital image providing a ‘true’ representation of the porous medium at a specified spatial resolution requires careful appraisal when the predicted results are generalized as representative of the original rock formation.

At present, we have in place efficient codes to calculate basic features of electrical conduction and fluid flow in image-based models of porous media.^{25,26} It is quite reasonable, therefore, to ask whether these codes could be applied directly to experimentally determined pore-space microgeometry. The objective of this paper is to benchmark pore-level calculations of absolute permeability, rel-

ative permeability, capillary pressure, and electrical resistivity performed on 3D micro-CT images of actual clastic rocks. One of the most important components of our work is the availability of laboratory measurements to quantify the sensitivity of the calculations to variations of image resolution, finite sample size, and presence and spatial distribution of clay, among other factors.

We consider three micro-CT images of quartzose sandstones (medium- to coarse-grained, moderately to poorly-sorted) with different petrophysical properties to perform both laboratory measurements and pore-level calculations. The study considers a systematic appraisal of rock properties and features of the simulation algorithm that could bias the calculations of petrophysical properties with pore-level methods. First, we briefly describe the numerical methods used to calculate rock properties in this study. Next, we describe the characteristics of both micro-CT images and laboratory measurements on the corresponding core samples. We will analyze the sensitivity of transport properties to variations of key computational parameters in the simulations, such as the number of random walkers, length of walk step, and the size of the simulated cubic sample. The calculated properties are compared to laboratory measurements performed on the corresponding core samples. Finally, we discuss the influence of both the spatial resolution of the micro-CT images and irreducible water saturation on the accuracy of the calculated macroscopic petrophysical properties.

Numerical Methods

A microstructure defined by a digital image is already discretized and readily lends itself to numerical computation of various properties. In this section, we briefly describe the numerical methods used to calculate absolute permeability, formation factor, and distribution of two-immiscible fluid phases in the micro-CT images of sedimentary rocks.

Calculation of absolute permeability The absolute permeability of a porous sample can be derived by numerically solving Stokes’ equation, which describes the steady-state flow of an incompressible Newtonian fluid in the limit of low Reynolds numbers, namely,

$$\mu \nabla^2 \mathbf{u}(\mathbf{x}) = \nabla p(\mathbf{x}), \quad \text{and} \quad (1)$$

$$\nabla \cdot \mathbf{u}(\mathbf{x}) = 0, \quad (2)$$

where \mathbf{u} and p are, respectively, the local velocity and pressure fields, μ is the fluid dynamic viscosity, and \mathbf{x} the position vector. At fluid-solid interfaces, the velocity \mathbf{u} satisfies the condition

$$\mathbf{u}(\mathbf{x}) = 0. \quad (3)$$

In addition, a macroscopic pressure gradient is applied at the inlet and outlet faces, whereas no-flow boundary conditions are enforced on the remaining faces of the sample. The permeability of the porous medium is calculated by volume averaging the local fluid velocity and applying Darcy’s equation.

We use a D3Q19 lattice-Boltzmann algorithm^{25,27} to simulate viscous flow of the single-phase fluid in the pore space of micro-CT images. In this study, we use the improved incompressible lattice-Boltzmann model²⁸ together with a pressure boundary condition²⁹ enforced on the inlet and outlet faces. To assess possible anisotropy of the images, simulations are performed individually for each of the x -, y - and z -directions. Absolute permeability is derived directly from the simulated velocity field using Darcy's equation. Effective absolute permeability is defined as the arithmetic average of the calculated absolute permeabilities in the x -, y -, and z -directions.

Calculation of formation factor. Steady-state flow of electric current through a porous medium saturated with an electrolyte is governed by the differential equation³⁰

$$\nabla \cdot [\sigma \nabla \Phi] = 0, \quad (4)$$

where Φ is the local electric potential. Additionally, a no-flux boundary condition is enforced at the solid-void interface when the solid phase is assumed to be insulating, *i.e.*,

$$\mathbf{n} \cdot \nabla \Phi = 0, \quad (5)$$

where \mathbf{n} is the unit normal vector outward from the solid to the pore space. The solution of this problem in terms of the electrical conductivity of the porous medium, σ_o , is given by

$$\langle \mathbf{j} \rangle = -\sigma_o \langle \nabla \Phi \rangle, \quad (6)$$

where $\langle \mathbf{j} \rangle$ and $\langle \nabla \Phi \rangle$ are the macroscopic electrical current density and potential gradient vectors, respectively.

The electrical conductivity of a porous sample is derived from the simulation of Brownian motion of diffusive particles (called walkers or random walkers) in the porous medium using a random-walk simulation algorithm.²⁶ Our implementation of the numerical algorithm was based on the calculation of the mean-squared displacement versus time for a number of Brownian particles taking discrete steps in the digital rock sample. In this model, many steps are taken with the direction of each step independent of the direction of the previous step. Calculation errors may be estimated by carrying out a series of independent random-walk simulations and performing a statistical analysis of the resulting distribution. This algorithm allows one to model arbitrary media boundaries, and takes into account the effect of clay minerals on the electrical conduction of shaly sands.

Calculation of relative permeability and resistivity index. In this study, we assume that the available micro-CT images (or core samples) are water-wet sandstones. Under such a condition, the wetting phase (water) occupies the corners of large pores and small pores, while the non-wetting phase (oil) occupies the central parts of the invaded pores. To assign spatial fluid distributions in the pore space, we implement the simple percolation algorithm proposed by Silin *et al.*^{31,32} to obtain several

distributions of wetting phase and non-wetting phase fluid for each sample, with each distribution corresponding to a different value of capillary pressure. The main idea behind this method is that one can calculate the curvature of the fluid-fluid interface in equilibrium at a given value of capillary pressure. Such an interface can be approximated by a spherical surface of the corresponding radius. Therefore, the part of the pore space occupied by the non-wetting phase can be represented as the union of all balls with this radius (or larger), which can be inscribed into the pore space. Fluid saturations are derived from the calculation of the volumes occupied by each fluid phase corresponding to a given value of capillary pressure.

The above procedure does not account for the history of fluid migration and hence only provides an approximate picture of fluid distribution. Therefore, the non-wetting fluid could be trapped at high values of saturation of the wetting phase, and the wetting fluid could be disconnected at low values of fluid saturation. In the simulation, we only consider the cases in which either the wetting phase or the non-wetting phase is connected in the pore space. Results presented here were mostly obtained under the assumption of no existence of water films on the grain surfaces. We will discuss the effect of such an assumption on simulation results, especially at low values of water saturation.

Equilibrium fluid distributions are used to calculate both relative permeability and resistivity index. For each case of water saturation modeled, we first compute the absolute permeability of the corresponding part of pore space occupied by each phase. The relative permeability of each phase is defined as the ratio of the absolute permeability at partial saturation to that at full saturation. On the other hand, the resistivity index is calculated from the ratio of the bulk electrical conductivity at full water saturation to that at partial water saturation, assuming that only the wetting phase is electrically conductive in the simulation.

Experimental Results

We consider three micro-CT images of quartzose sandstones (medium- to coarse-grained, moderately to poorly-sorted) with different petrophysical properties to perform pore-level calculations of permeability, relative permeability, capillary pressure, and electrical conductivity. These images have the same size of $300 \times 300 \times 300$ voxels with the side length of each voxel equal to 4.5 microns. Voxel-based porosities (the ratio of the number of voxels in the void space to the total number of voxels) of these CT images are 21.1%, 14.5%, and 10.4%, respectively. We label these images (or core samples) as CTA, CTB and CTC in decreasing order of porosity. **Figure 1** is an example of the pore space associated with the CTA micro-CT image.

Laboratory measurements were performed on the corresponding core samples before the micro-CT images were acquired via X-ray computed tomography. **Table 1** lists part of the experimental measurements. Measured values of relative permeability, capillary pressure, and resistivity will be shown for comparison against simulation results in the next section.

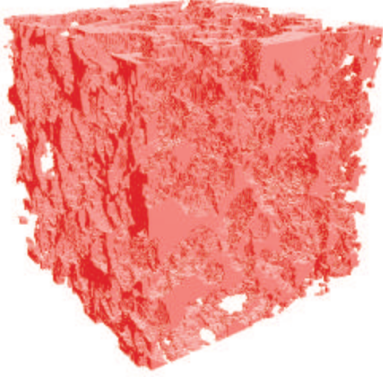


Figure 1— Pore space of the micro-CT image CTA with a porosity equal to 21.1%. The number of voxels is $300 \times 300 \times 300$. Voxel resolution is $4.5 \mu\text{m}$.

Table 1— Measured value of porosity ϕ_e (%), formation factor F_e , air permeability k_e (mD), and end-point oil permeability k_o^0 (mD) at irreducible water saturation S_{wi} (%) for the core samples associated with available micro-CT images. Porosities of CT images, ϕ_s , are also listed for comparison.

	ϕ_s	ϕ_e	F_e	k_e	k_o^0	S_{wi}
CTA	21.1	20.3	17.5	59.1	42	21.7
CTB	14.5	15.4	31.8	957	952	9.1
CTC	10.4	12.1	55.8	191	132	22.5

Numerical Results and Analysis

In this section, we apply our numerical simulation methods to calculate flow properties of three micro-CT images, including absolute permeability, formation factor, relative permeability, capillary pressure, and resistivity index. Results are compared to laboratory measurements performed on the corresponding core samples. The effect of irreducible water saturation, S_{wi} , on the calculated results is investigated in detail. We first analyze the sensitivity of formation factor to variations of key computational parameters in the random-walk simulations, the number of walkers and the length of a walk step. Also, we study how the size of the simulated cubic sample affects the calculated rock properties. This study is performed to ensure that the size of the simulated sample is large enough to yield representative results.

Influence of the length of walk steps and the number of walkers. In the random-walk simulation, the computed formation factor depends on both the length of walk steps and the number of walkers. Walkers (or particles) randomly migrate via discrete steps through the detailed microscopic structure of porous media. In the long-time limit, walkers fully experience the tortuosity of the pore space. The diffusion coefficient of a porous sample, measured at long simulation times, is defined by the time derivative of the mean squared displacement, $\langle r^2(t) \rangle$, of a collection of walkers. Through the tortuosity, the dif-

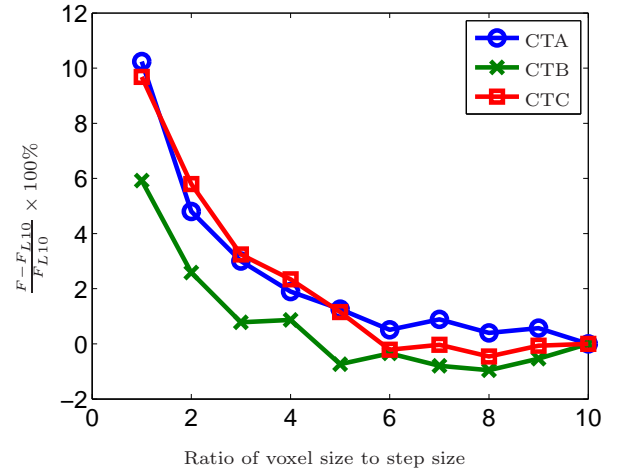


Figure 2— Effect of step size on the calculated formation factor of CT images. Each data point represents the mean value of 10 independent random-walk simulations, each consisting of 2000 walkers. For each simulation, we calculated the corresponding formation factor. The variable F_{L10} is the mean value of 10 independent simulations performed with a step size equal to $1/10$ of voxel size. Refer to Table 1 for a description of core samples under consideration.

fusion coefficient is intimately connected to the electrical conductivity of porous media^{33–35}

In principle, accurate simulation results could be obtained with very small step sizes and a large number of walkers. However, this strategy may not be computationally efficient for the simulation of a large porous system. A small decrease in step size leads to a large increase in computer time. In order to determine suitable values for step size and number of walkers, we conducted a series of simulations on the three micro-CT images.

Figures 2 and 3 show the dependence of the calculated formation factor on both the step size and the number of walkers. Each data point in Figure 2 describes the mean value of 10 independent random walk simulations, each consisting of 2000 walkers. The formation factor was calculated for each simulation. We assume that the formation factor obtained with a small step size equal to $1/10$ of the voxel size is the ‘true’ value of the CT image, denoted by F_{L10} . One observes that the calculated formation factor decreases as the step size decreases. Once the ratio of voxel size to step size exceeds 5, the calculated formation factor is within 1% of the ‘true’ value, F_{L10} . Thus, we choose a step size equal to $1/10$ of the voxel size for the remaining simulations.

For reasons of computation time and accuracy, it is important to use an optimum number of walkers to simulate pore-level phenomena that govern electrical conduction in porous media. Figure 3 describes the dependence of the calculated formation factor on the number of walkers used in the simulation. For comparison, we assume that the computed formation factor from the simulations consisting of 3000 walkers is the ‘accurate’ result, denoted by

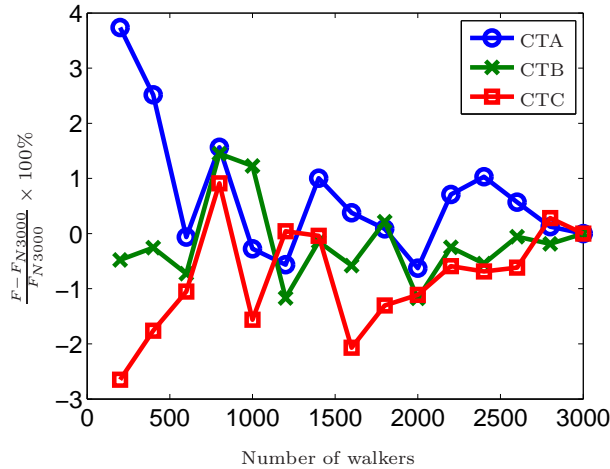


Figure 3— Effect of the number of walkers on the calculated formation factor of CT images. Each data point represents the mean value of 10 independent random-walk simulations. For each simulation, we calculated the formation factor. The variable F_{N3000} describes the mean value of 10 independent simulations, each consisting of 3000 walkers. Step size is equal to 1/10 of voxel size. Refer to Table 1 for a description of core samples under consideration.

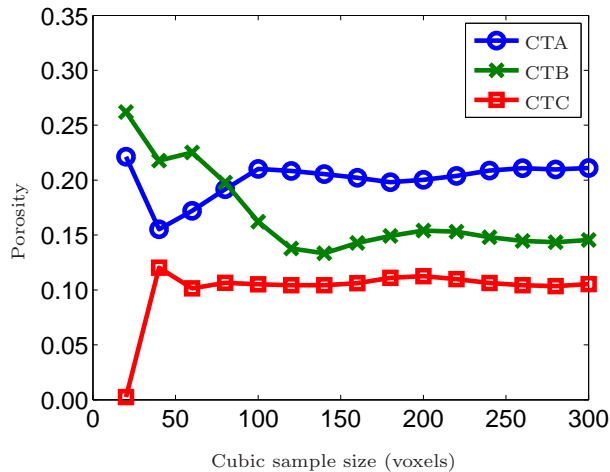


Figure 4— Variation of porosity with the cubic sample size for three CT images. Sample size is described in terms of voxels, whose size is 4.5 microns. Refer to Table 1 for a description of core samples under consideration.

F_{N3000} . Simulation results did not exhibit significant variations (within ± 1 of F_{N3000}) once the number of walkers exceeded 1000. Based on the above result, we have chosen to use 2000 walkers in every case for all the simulations reported in the paper.

Effect of sample size. To simulate fluid flow through a rock sample, we wish to choose the sample size as large as possible. However, due to limited computer power, the simulation sample size should be small enough to be computationally feasible. Errors will occur if we use a sample

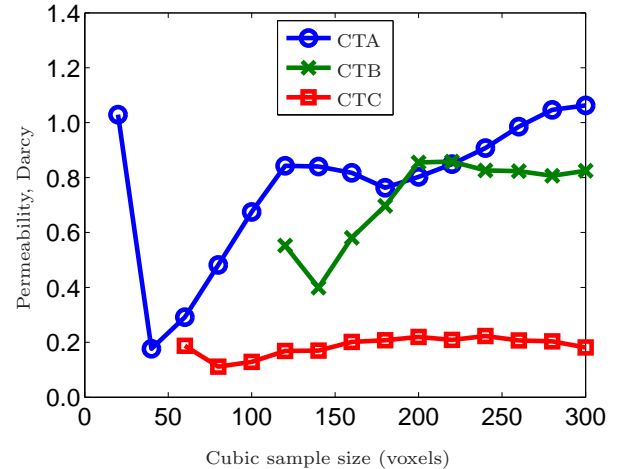


Figure 5— Effect of cubic sample size on the calculated absolute permeability of CT images. Sample size is described in terms of voxels, whose size is 4.5 microns. Each data point describes the arithmetic-average permeability in the x -, y -, and z -directions. Refer to Table 1 for a description of core samples under consideration.

that is too small to calculate the corresponding macroscopic properties, and the properties of a small sample may not be representative of the original rock formation. To reach a compromise, we study how the size of the simulated sample affects the calculated values of porosity, absolute permeability, and formation factor on the micro-CT images. The objective is to determine the size of the simulated sample which is large enough to give reliable results but still small enough for computational purposes.

Figures 4, 5, and 6 describe the effect of cubic sample size on the calculated porosity, absolute permeability and formation factor for the three micro-CT images, respectively. The simulated sample is located at the center of the image. Sample size is expressed in terms of voxels. To assess possible permeability anisotropy of the rock, simulations are performed individually for each of the x -, y - and z -directions and the permeability is obtained in these three directions. However, only the arithmetic-average permeability is shown in Figure 5.

One observes that both porosity and formation factor fluctuate rapidly when the size of the cubic sample is small, but approach their respective constants with increasing sample size. However, sample sizes necessary for the porosity and formation factor to reach a constant value are different for different images. On the other hand, the permeability of images CTB and CTC approach their respective constant values with increasing cubic sample size, while the permeability of image CTA fails to reach an asymptote. This result highlights potential problems as the calculated value obtained on a small cubic sample may no longer be representative. Thus, to calculate petrophysical properties of micro-CT images, we will use the original sample size of $300 \times 300 \times 300$ voxels.

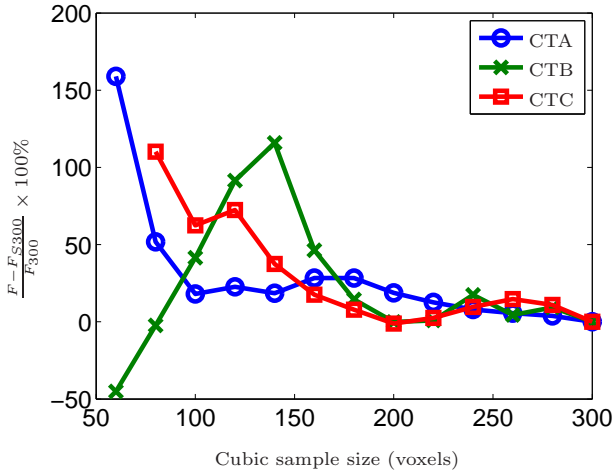


Figure 6— Effect of the cubic sample size on the calculated formation factor of CT images. Sample size is described in terms of voxels, whose size is 4.5 microns. F_{S300} is the calculated formation factor of CT images with $300 \times 300 \times 300$ voxels. Refer to Table 1 for a description of core samples under consideration.

Table 2— Calculated values of permeability and formation factor for three micro-CT images compared to laboratory measurements made on the corresponding core samples. Variables k_x , k_y , and k_z , are the calculated permeability (Darcy) in the x -, y -, and z -directions, respectively. The variable k_a is the average permeability value, $(k_x + k_y + k_z)/3.0$. Measured permeability is denoted by k_e . Computed and measured formation factors are denoted by F_s and F_e , respectively. Note that sample CTA is a shaly sand.

	k_x	k_y	k_z	k_a	k_e	F_s	F_e
CTA	1.08	1.18	0.92	1.06	0.06	18.5	17.5
CTB	0.80	0.84	1.04	0.89	0.96	37.1	31.8
CTC	0.14	0.23	0.17	0.18	0.18	77.8	55.8

Absolute permeability and formation factor. In Table 2, we compare the computed absolute permeability and formation factor of micro-CT images against experimentally measured values. Absolute permeabilities of images CTB and CTC are in good agreement with the measured values while image CTA has a too high calculated value. We note that the calculated rock absolute permeability is different in the three orthogonal directions for all three CT images, *i.e.*, they are anisotropic. The x -, y -, and z -directions are labeled only for convenience. In reality, we do not know the exact vertical (gravity) and horizontal directions for these images. For this type of anisotropic rock, it is important to know how the formation was sampled for proper assessment of laboratory measurements and/or numerical results.

A possible explanation for the extremely high calculated value of absolute permeability of image CTA is that it is a shaly sand in which clays have pore-lining or pore-bridging characteristics, and that these fine clays can not

Table 3— Values added to the calculated water saturation in order to make the simulated curves match laboratory measurements. The new water saturation is $S_w + xS_{wi}$, where S_w is the originally calculated water saturation, and S_{wi} is the measured irreducible water saturation of core samples.

	S_{wi}	$x(P_c)$	$x(k_{rw})$	$x(k_{ro})$	$x(I_R)$
CTA	21.7	+2.0	-0.5	+0.5	-0.5
CTB	9.1	+2.0	-1.0	+1.0	-1.0
CTC	22.5	+1.0	0.0	+1.0	-0.5

be detected in the digital image at a spatial resolution of 4.5 microns. It is well known that lining or bridging clay morphology is responsible for partial to complete fluid-flow barriers that can seriously impair rock permeability, even for sands of relatively high porosity and low clay content.^{36–38}

On the other hand, the predicted formation factor is consistent with experimental measurements for all three images. In general, we observe an overestimation of the calculated formation factor. The fact that our calculations overestimate the formation factor may be due to several possible reasons: (1) The image size is smaller than the size of the corresponding core sample, approximately an order of magnitude difference in linear dimension; (2) image resolution is not high enough, which does not allow for an accurate representation of the smaller pores and throats. On physical grounds, we do not expect these channels to contribute greatly to fluid flow (absolute permeability), but their effect on electrical conduction can be substantial;^{22,26,39} (3) we did not consider the effect of clay minerals on the simulation of transport properties. Laboratory measurements confirmed that a small amount of clay was present in the core samples. However, the digital image itself could not differentiate the types of corresponding core samples, clay mineral-free sands or shaly sands. It is well recognized that presence of clay minerals could dramatically affect flow properties,^{37,40} thereby resulting in higher electrical conductivity and lower absolute permeability and formation factor. We will discuss the effect of image resolution and presence of clay minerals (or irreducible water distribution) on the calculated results in a subsequent section.

Capillary pressure. Figure 7 shows the calculated capillary pressure curves for the three images, together with the corresponding measurements performed on core samples. Simulation curves were shifted to match laboratory measurements by adding an extra value in the computed water saturation S_w , *i.e.*,

$$S_w + xS_{wi} \rightarrow S_w, \quad (7)$$

where S_{wi} is the measured irreducible water saturation of core samples. Specific values of x are listed in Table 3.

The capillary pressure curve was calculated without considering the history of fluid migration. Implicitly, it is assumed that the pore space is initially saturated with the

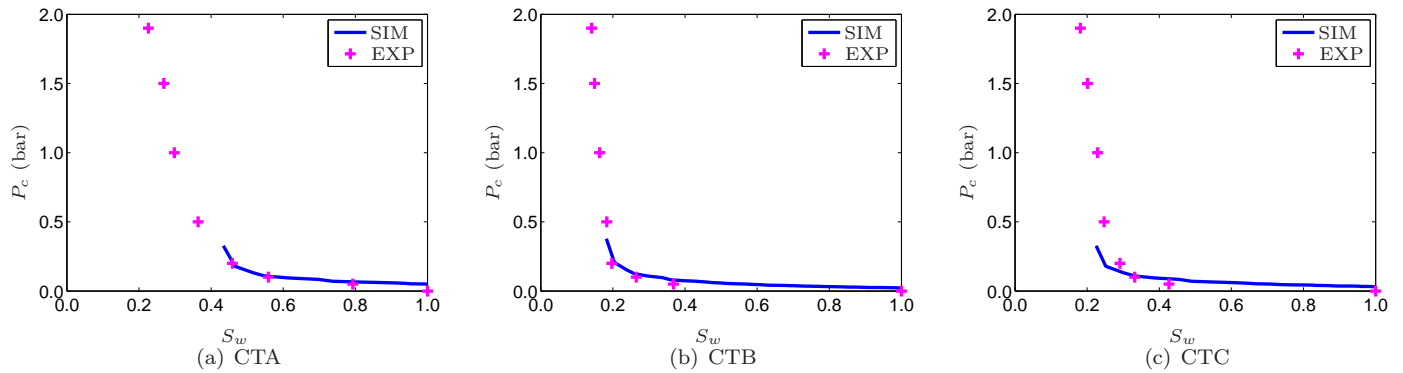


Figure 7— Pseudo capillary pressure curves calculated from simulations performed on three micro-CT images via the simple percolation algorithm. Simulation curves were shifted to match laboratory measurements by adding a constant to the calculated water saturation. Values added to the calculations are listed in Table 3.

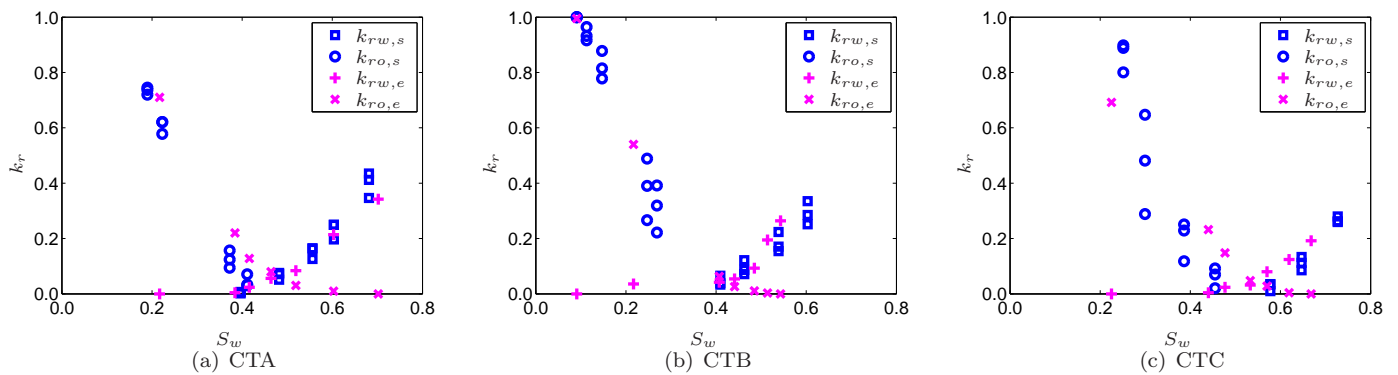


Figure 8— Calculated relative permeability curves of CT images compared to measurements performed on the corresponding core samples. Calculated relative permeability values were shifted to match experimental measurements by adding a constant value to the calculated water saturation. Values added to the calculations are listed in Table 3.

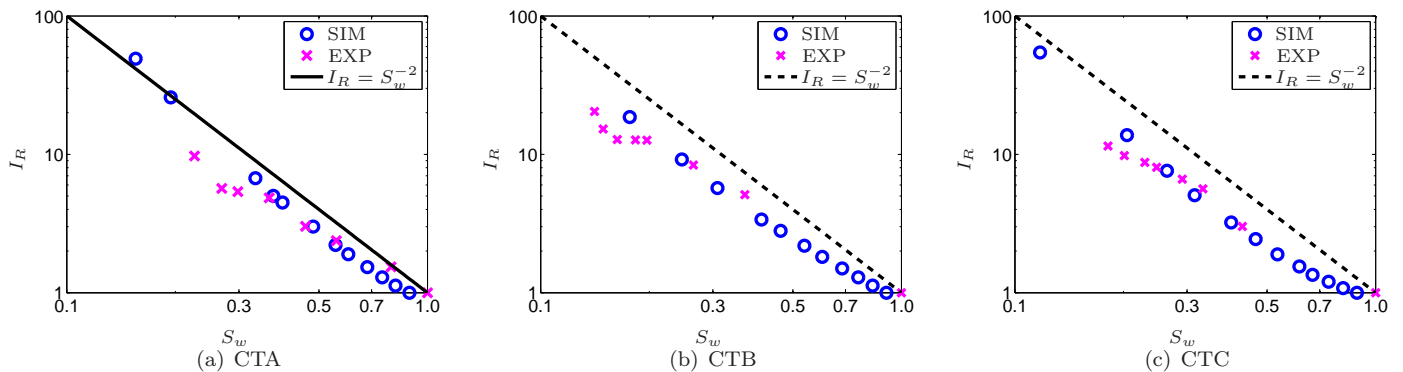


Figure 9— Calculated resistivity index of CT images compared to measurements performed on the corresponding core samples. Calculated values of water saturation were modified by adding a constant in order to match laboratory measurements. Values added to the calculations are listed in Table 3.

non-wetting phase. Thus, the computed curves better reflect the imbibition capillary pressure rather than those of primary drainage.⁶

In the simulations, we assumed that the pore space of CT images was completely occupied by wetting and non-wetting phases, both of which are moveable. This assumption implies that no irreducible wetting phase was considered, that is $S_{wi} = 0$. However, presence of clay within the core samples results in a higher value of irreducible water saturation (see Table 3), although part of the water in the pore space could be further displaced at higher pressure. Therefore, corrections should be applied to account for clay-bound water saturation, that is the reason why we shifted the computed curves as described by Equation (7). One can find that, to match the measurements, the values of x for the shifted saturation values are different for the three images. This behavior may be explained by different types of clay present in the core samples. It is well known that different clay morphologies significantly affect rock porosity/permeability, capillary pressure curve, and associated pore-size distributions in different ways.³⁷ At present, we do not have specific information concerning clay types for core samples under consideration.

In addition, one can observe that there is no calculated low values of water saturation. It is intuitively evident that a portion of the pore space, such as small pores or micro-pores within the clay fraction, are not resolved by the micro-CT images at a resolution of 4.5 microns. These small pores may still connect to the large pore space. It would be necessary to exert a higher pressure if water filled within these pores were to be displaced. In the simulation, only large pores present at the resolution of 4.5 microns are considered for the calculation of properties. This fact is reflected in Fig. 7 by the observation that our simulations approximately match measurements at high values of water saturation. We expect that, due to the limit of image resolution, a systematic error will occur for high values of capillary pressure. More accurate calculations require higher image resolution, especially for the case of complex rock samples, such as those associated with shaly sands.

Relative permeability. To calculate the relative permeability, we first calculate the absolute permeability of each configuration of the pore space occupied by either the wetting (water) or non-wetting phase (oil) obtained at different values of capillary pressure. The saturation is calculated for the same fluid configuration for which the capillary pressure is applied. Relative permeability is calculated by dividing the absolute permeability of each configuration by the absolute permeability of the whole pore space image. **Figure 8** displays the computed and measured values of relative permeability for the three CT images. The calculated relative permeability was shifted to match laboratory measurements with consideration of irreducible water saturation resulting from presence of clay in the core samples. Table 3 lists the shifted values of x in Equation (7).

We did not calculate the relative permeability of water or oil at low values of their saturation, in which the pore space occupied by either water or oil is disconnected, or even if it is connected, because in such a situation the available image resolution is not high enough for the lattice-Boltzmann flow simulation to warrant accurate results. In reality, when the non-wetting phase occupies the centers of invaded pores, the wetting phase may reside in grooves, crevices, or roughness in the pore space. Wetting layers are stabilized by capillary forces and have a typical thickness of a few microns – comparable to, although smaller than – the size of the pores. Flow through these layers, albeit slow, is measurable and can have a significant impact on fluid displacement.⁴¹

Fluid phase configurations were a direct result of the computation of capillary pressure curves described in the previous section. Therefore, all related assumptions and explanations are applicable to the computation of relative permeability. In addition, since relative permeability was calculated as the ratio of two calculated values of absolute permeability from digital images, we expect that errors due to image discretization and numerical algorithm should be negligible, and that the shape of calculated relative permeability curves should be similar to that of measured curves. **Figure 8** confirms this explanation and implies that fluid phase distributions obtained with the simple percolation algorithm are reliable, although they provide only an approximate description of spatial fluid distributions.

Resistivity index. The resistivity index is calculated in a similar manner to the calculation of relative permeability: We calculate the electrical conductivity for each configuration of the pore space occupied by the conductive fluid phase (water) at different values of capillary pressure (or water saturation). The resistivity index is defined as the ratio of the conductivity of the rock fully saturated with water to the conductivity of the same rock partially saturated with water.⁴² **Figure 9** shows the computed resistivity index as a function of water saturation, together with the corresponding measurements performed on core samples. The calculated water saturation was modified using Equation (7) to take into account irreducible water saturation, in an effort to make the simulation curve approximately match laboratory measurements. There are few experimental measurements available at high values of water saturation.

We observe that values of x listed in Table 3 are different for capillary pressure, relative permeability, and resistivity index even for the same image. Our explanation is as follows: Capillary pressure is very sensitive to the rock's pore-size distribution. Pores smaller than 4.5 micron resolution are not resolved by the available CT images. The effect of these small pores on the capillary pressure curve is reflected on the portion of the curve at low values of water saturation. Our simulations better reflect the effect of larger pores, *i.e.*, the segment of the curve at high value of water saturation. However, in **Figure 7**, we attempted to match the overall simulated shape to laboratory mea-

surements, thereby resulting in a larger value of x , even though the calculations at low values of water saturation may not be reliable.

Our simulations did not account for the effect of clay on resistivity index. Clay minerals themselves may not be very conductive, but ionic substitution within the clay lattices causes an excess of cations in the pore fluid immediately adjacent to clay surfaces. The result is abnormally high conductivity near clay surfaces, which can contribute substantially to the electrical conductivity of the whole porous systems at low values of salinity or/and high temperature.^{30,40,43-45} This effect will become more significant at low values of water saturation.^{26,39,46} We discuss the effect of presence of clay on the calculated resistivity index in the next section.

Effect of voxel resolution and presence of clay on the calculated rock properties.

In the previous sections, we described rock flow properties calculated from three available CT images. These results were obtained without consideration of either the effect of image resolution or presence of clay minerals. In what follows, we investigate how the two factors affect the numerical simulations. A small cubic sample extracted from the center of image CTA is used to illustrate this point.

Due to limited computer power, we extract a small cubic sample with a linear size of 100 voxels from the center of the CTA image. This small sample is labeled CTA₅. We know from Fig. 5 that the size of CTA₅ is too small and hence its properties may not be representative of the whole image CTA or of the original rock formation. However, its small size allows us to increase the spatial resolution from 4.5 microns to 2.25 and 1.125 microns, while the simulations on the new sample size are still computationally feasible. We increase the spatial resolution of the image CTA₅ by replacing each original voxel in the image with 8 ($2 \times 2 \times 2$) or 64 ($4 \times 4 \times 4$) finer voxels of the same phase (solid or void space), thereby doubling image resolution but still leaving the geometry of the image intact. The new sample sizes are $200 \times 200 \times 200$ and $400 \times 400 \times 400$ voxels with the linear size of each voxel equal to 2.25 and 1.125 microns, respectively.

Table 4 summarizes the effect of image resolution on the calculated absolute permeability and formation factor for sub-image CTA₅. Due to limitations of computer power, we did not calculate absolute permeability for the sample with a resolution of 1.125 microns. One can observe that image resolution has negligible or little effect on the calculated results. This is due to the fact that the increase of spatial resolution does not change the geometry of the pore space of the digital image. Small pore spaces or flow channels in the core samples can only be resolved with higher resolution during X-ray CT image acquisition. In this context, attempts^{16,17} to develop efficient procedures of computer reconstruction of sedimentary rocks will be a good alternative to improve calculations, since they allow one to create the corresponding digital image with an arbitrary high degree of spatial resolution.²⁵

Table 4— Effect of image resolution a (microns) and simulated irreducible water saturation $S_{wi,s}$ (%) on the calculated values of absolute permeability and formation factor for sub-image CTA₅. Variables k_x , k_y , and k_z , are the calculated permeability (Darcy) in the x -, y -, and z -directions, respectively. Variable k_a is the average permeability, $(k_x + k_y + k_z)/3.0$. The computed formation factor is denoted by F_s .

a	$S_{wi,s}$	k_x	k_y	k_z	k_a	F_s
4.500	0.00	0.96	0.66	0.40	0.67	21.7
2.250	0.00	0.93	0.67	0.43	0.68	21.6
2.250	36.5	0.16	0.08	0.05	0.10	21.7
1.125	0.00	-	-	-	-	21.6
1.125	18.7	-	-	-	-	21.6
1.125	36.5	-	-	-	-	21.7

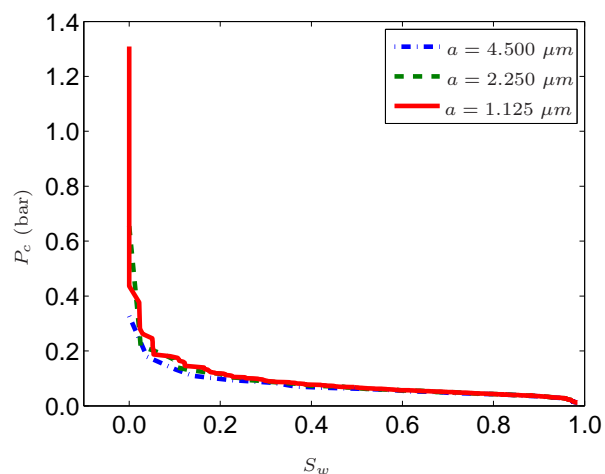


Figure 10— Effect of voxel size on the calculated capillary pressure curves of sub-CT image CTA₅ extracted from the center of CT-image CTA.

Similar conclusions can be drawn from capillary pressure curves calculated for different image resolutions, shown in **Figure 10**. We find that the overall shape of the curve is not affected by the discretization. The difference at end-points of high pressure is caused by numerical error associated with the determination of pore sizes, not by the discretization itself. Since we did not change the geometry of the pore space in the process, the pore size distribution should be the same, and the finer voxels originating from the same coarse voxel will continue to belong to the same pore. However, in the numerical calculation, a finer voxel could belong to another pore due to numerical errors. This behavior is reflected by the difference of values calculated at the end-points, which are inversely proportional to the corresponding image resolution.

Presence of clay minerals in the samples could have a substantial effect on both fluid flow and electrical conduction. Fluid flow is in most cases controlled by the large connected flow channels in the sample, whereas small connected channels contribute little to absolute permeability.

However, electrical conduction of a porous sample will benefit from the contribution of all connected flow channels.²² Disregarding presence of clay minerals will result in abnormally high permeability and formation factor (or low electrical conductivity; see the computed values for image CTA in Table 2).

To investigate the effect of clay on rock properties, we have chosen to use a “simple” grain coating model to simulate clay morphology in the sample,^{47,48} in which pore-lining clays are attached to pore walls to form a relatively continuous and thin clay-mineral coating shell with thickness δ . We assume that the clay-coating shell has a very high porosity, but that its permeability is still negligible due to the very small pore-size distribution. Therefore, we treated the clay shell as microporous, but as impermeable solid phase in the simulation of fluid flow. However, since micropores included in this shell are capable of holding irreducible water, we treated the shell in the simulation of electrical conduction as the cumulative electrical effect from surface phenomena due to the corresponding double layer.²⁶

Table 4 describes the effect of the clay shell on the calculated absolute permeability and formation factor. We find that presence of pore-lining or pore-bridging clays dramatically reduces the permeability of image CTA₅, while its effect on electrical conductivity is negligible when the sample is fully saturated. Therefore, presence of clays in the sample CTA could explain its relatively high porosity and its low absolute permeability, which also implies that clays could exhibit either pore-lining or pore-bridging morphology.

While the effect of clay minerals on electrical conductivity is negligible at high values of water saturation, its influence becomes more significant at low values of water saturation. **Figure 11** shows the variation of the computed resistivity index with water saturation for the same image with different thickness of the clay-coating shell. The volume of the clay shell is calculated from irreducible water saturation, S_{wi} . Surprisingly, the calculated resistivity index is in excellent agreement with measurements when clay-bound water is taken into account in the simulation. The very good agreement between simulations and measurements confirms that the amount of clay-bound water indeed should not be negligible in the simulation.

In addition, the rough grain surface resulting from presence of clay minerals in the sample does indeed result in a lower value of the saturation exponent included in Archie’s equation.⁴² This observation follows from our simulation results in Figure 11 and from those of earlier studies.^{26,39,46} Such behavior can be explained by considering that the rough surface due to clay morphology will retain a relatively thick and continuous water layer through capillary forces, thereby providing a favorable path for electrical conduction.

Discussion and Conclusions

We presented systematic pore-level calculations of rock petrophysical properties, including absolute permeability,

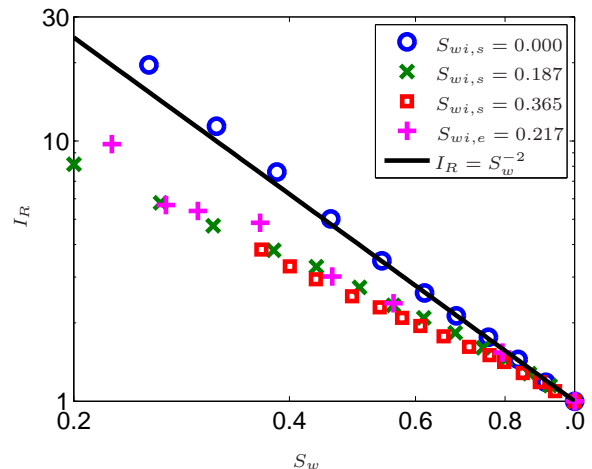


Figure 11— Effect of irreducible water saturation (S_{wi}) on the calculated resistivity index of the sub-CT image CTA₅ extracted from the center of CT-image CTA. The size of CTA₅ is increased from 100^3 to 400^3 by replacing each original voxel (resolution $4.5 \mu\text{m}$) with 64 ($4 \times 4 \times 4$) finer voxels (resolution $1.125 \mu\text{m}$) of the same phase (solid or void space). Irreducible water is uniformly distributed on the solid surface.

relative permeability, capillary pressure, and resistivity index of three 3D micro-CT images of clastic rocks. Absolute permeability was calculated with the lattice-Boltzmann method, whereas formation factor was calculated with a random-walk technique. Immiscible two-phase fluid distributions in the pore space were approximately determined using a simple percolation algorithm while enforcing capillary equilibrium.

Our numerical algorithms were successfully tested and validated by comparisons between simulations and laboratory measurements. Pore-level calculations agreed well with the corresponding laboratory measurements when immovable fluid saturation of the wetting phase was taken into account. This good agreement indicated that our pore-level approaches were reliable to calculate rock properties directly on experimentally determined pore-space microgeometry.

We also studied the sensitivity of the computed rock properties to several key simulation factors, including the length of walk steps, the number of walkers, the simulated sample size, spatial image resolution, and presence of clay minerals. We found that the computed electrical conductivity does depend on both the walk step size and the number of walkers used in the simulation. However, their influence can be negligible by careful selection of these parameters. Our studies also showed that calculated rock properties from images varied with the simulated sample size, especially for sample CTA containing a significant amount of clay minerals. This behavior implies that a representative elementary volume could not be obtained and that the calculation performed on a small cubic sample may no longer be representative of the original rock formation.

The dependence of the computed results on image resolution was investigated by refining the existing data sets through replacement of each original voxel in the image with 2^3 and 2^6 finer voxels of the same phase (solid or void space). Our simulations showed that there was little effect on the calculated properties resulting from the artificial increase of image resolution. This result is consistent with our expectation since the increase of image resolution does not change the geometry of the digital image. On the other hand, we believe that image resolution does affect the comparison between numerical results obtained from the digital image and measurements performed on core samples. We could not detect all textural and geometrical details of core samples using X-ray computed tomography at the available spatial resolution. Often, dismissing finer structure could result in a completely different result, similar to the example of the CTA image considered in our study. As an alternative, numerical approaches^{16,17} used to reconstruct the microstructure of porous media can be used to improve the reliability of the calculation, since they allow the construction of digital images with an arbitrary degree of spatial resolution.²⁵

Clay minerals, which are present in most clastic reservoir rocks, exert a major control on reservoir quality. Permeability, water saturation, and electrical conductivity are particularly sensitive to presence of clay minerals. Micropores including in clay shells are capable of holding significant amount of irreducible water, which results in substantially higher electrical conductivity and lower permeability.^{36,37} A 3D digital image acquired at a specific spatial resolution cannot provide textural information with the necessary spatial resolution. We used a "simple" grain-coating model to simulate clay morphology in the sample,^{47,48} and our simulations indicated that the amount of clay-bound water cannot be neglected in pore-level petrophysical calculations.

The accuracy of numerical calculations critically depends on the quality of input data – the 3D micro-CT images. With no guarantee that the geometry of the digital pore space is close to the real system, there will be little confidence that numerical techniques could be used to reliably predict rock properties. For rocks containing significant amounts of clay minerals, such as sample CTA in our study, a resolution of 4.5 microns may not be enough to detect the finer 3D pore structure (smaller pores and throats) within clays, which still contribute substantially to fluid flow and electrical conduction. Higher image resolution is needed to appraise the macroscopic petrophysical properties of such rock samples. Future simulations will be validated using synchrotron micro-CT images with a resolution of 1.4 microns.

For the simulation of two-phase fluid flow inside the pore space of micro-CT images, it is important to determine the geometrical regions occupied by the wetting and non-wetting fluid phases at a given value of capillary pressure. We used a simple percolation algorithm to approximately determine the spatial fluid-phase distributions in the digital pore space. However, this procedure did not model

the physical process of imbibition or drainage. We are currently in the process of developing a new simulation algorithm based on previous approaches^{31,49,50} to model primary drainage for a completely wetting system, including the effect of water films and clay-bound water.

The promising results stemming from our study confirm the feasibility of combining X-ray micro-CT images with pore-level numerical simulations to accurately and reliably predict petrophysical properties of individual rock morphologies. We conclude by noting that some of the preliminary observations presented here can only be verified with a detailed study of a large number of pore-level simulations of digital images and laboratory measurements.

Acknowledgements

The work reported in this paper was funded by the University of Texas at Austin's Research Consortium on Formation Evaluation, jointly sponsored by Aramco, Baker Atlas, BHP Billiton, BP, British Gas, ConocoPhillips, Chevron, ENI E&P, ExxonMobil, Halliburton Energy Services, Hydro, Marathon Oil Corporation, Mexican Institute for Petroleum, Occidental Petroleum Corporation, Petrobras, Schlumberger, Shell International E&P, Statoil, TOTAL, and Weatherford.

The authors acknowledge the Texas Advanced Computing Center (TACC) at The University of Texas at Austin for providing high performance computing resources that have contributed to the research results reported in this paper. We are also thankful to Professor Tad W. Patzek of the University of California at Berkeley and Dr. Dmitriy B. Silin of Lawrence Berkeley National Laboratory for their help in displaying the 3D micro-CT images.

References

- [1] Pal-Eric Øren and Stig Bakke. Process based reconstruction of sandstones and prediction of transport properties. *Transport in Porous Media*, 46(2-3):311–343, 2002.
- [2] Brian P. Flannery, Harry W. Deckman, Wayne G. Roberge, and Kevin L. D'Amico. Three-dimensional X-ray microtomography. *Science*, 237(4821):1439–1444, 1987.
- [3] J. T. Fredrich, B. Menendez, and T.-F. Wong. Imaging the pore structure of geomaterials. *Science*, 268(5208):276–279, 1995.
- [4] M. E. Coles, R. D. Hazlett, E. L. Muegge, K. W. Jones, B. Andrews, B. Dowd, P. Siddons, A. Peskin, P. Spanne, and W. E. Soll. Developments in synchrotron X-ray microtomography with applications to flow in porous media. In *Annual Technical Conference and Exhibition*, Denver, Colorado, USA, 1996.
- [5] D. Wildenschild, J. W. Hopmans, C. M. P. Vaz, M. L. Rivers, D. Rikard, and B. S. B. Christensen. Using X-ray computed tomography in hydrology: systems, resolutions, and limitations. *Journal of Hydrology*, 267(3-4):285–297, 2002.
- [6] Liviu Tomutsa and Dmitriy B. Silin. Nanoscale pore imaging and pore scale fluid flow modeling in chalk. In *25th Annual Workshop and Symposium Collaborative Project on Enhanced Oil Recovery*, Stavanger, Norway, 2004.

- [7] M. Joshi. *A class of stochastic models for porous media*. PhD Dissertation, University of Kansas, 1974.
- [8] Jacques A. Quiblier. A new three-dimensional modeling technique for studying porous media. *Journal of Colloid and Interface Science*, 98(1):84–102, 1984.
- [9] P. M. Adler, C. G. Jacquin, and J. A. Quiblier. Flow in simulated porous media. *Int. J. Multiphase Flow*, 16(4):691–712, 1990.
- [10] J. Salles, J. F. Thovert, and P. M. Adler. Reconstructed porous media and their application to fluid flow and solute transport. *Journal of Contaminant Hydrology*, 13(1-4):3–22, 1993.
- [11] C. L. Y. Yeong and S. Torquato. Reconstructing random media, II. Three-dimensional media from two-dimensional cuts. *Physical Review B*, 58(1):224–233, 1998.
- [12] S. Bekri, K. Xu, and F. Yousefian. Pore geometry and transport properties in North Sea chalk. *Journal of Petroleum Science and Engineering*, 25:107–134, 2000.
- [13] James N. Roberts and Lawrence M. Schwartz. Grain consolidation and electrical conductivity in porous media. *Physical Review B*, 31(9):5990–5998, 1985.
- [14] Lawrence M. Schwartz and Stephen Kimminau. Analysis of electrical conduction in the grain consolidation model. *Geophysics*, 52(10):1402–1411, 1987.
- [15] S. L. Bryant, Christopher Cade, and David Mellor. Permeability prediction from geologic models. *The American Association of Petroleum Geologists Bulletin*, 77(8):1338–1350, 1993.
- [16] Stig Bakke and Pal-Eric Øren. 3-D pore-scale modelling of sandstones and flow simulations in the pore networks. *SPE Journal*, 2:136–149, 1997.
- [17] Guodong Jin, Tad W. Patzek, and Dmitriy B. Silin. Physics-based reconstruction of sedimentary rocks. In *SPE Western Regional/ AAPG Pacific Section Joint Meeting*, Long Beach, California, USA, 2003.
- [18] D. Coelho, J.-F. Thovert, and P. M. Adler. Geometrical and transport properties of random packings of spheres and aspherical particles. *Physical Review E*, 55(2):1959–1978, 1997.
- [19] Laurent Tacher, Pierre Perrochet, and Aurele Parriaux. Generation of granular media. *Transport in Porous Media*, 26:99–107, 1997.
- [20] Marco Pilotti. Generation of realistic porous media by grain sedimentation. *Transport in Porous Media*, 33:257–278, 1998.
- [21] P. Spanne, J. F. Thovert, C. J. Jacquin, W. B. Lindquist, K. W. Jones, and P. M. Adler. Synchrotron computed microtomography of porous media: topology and transport properties. *Physical Review Letters*, 73(14):2001–2004, 1994.
- [22] F. M. Auzerais, J. Dunsmuir, B. B. Ferrol, N. Martys, J. Olson, T. S. Ramakrishnan, D. H. Rothman, and L. M. Schwartz. Transport in sandstone: a study based on three dimensional microtomography. *Geophysical Research Letters*, 23(7):705–708, 1996.
- [23] Christoph H. Arns, Mark A. Knackstedt, W. Val Pinczewski, and W. B. Lindquist. Accurate estimation of transport properties from microtomographic images. *Geophysical Research Letters*, 28(17):3361–3364, 2001.
- [24] Thierry Bourbie and Bernard Zinszner. Hydraulic and acoustic properties as a function of porosity in Fontainebleau sandstone. *Journal of Geophysical Research*, 90(B13):11524–11532, 1985.
- [25] Guodong Jin, Tad W. Patzek, and Dmitriy B. Silin. Direct prediction of the absolute permeability of unconsolidated and consolidated reservoir rock. In *SPE Annual Technical Conference and Exhibition Meeting*, Houston, Texas, USA, 2004.
- [26] Guodong Jin, Carlos Torres-Verdín, Sarath Devarajan, Emmanuel Toumelin, and E. C. Thomas. Pore-scale analysis of the Waxman-Smiths shaly-sand conductivity model. *Petrophysics*, 48(2):104–120, 2007.
- [27] Guodong Jin. *Physics-based modeling of sedimentary rock formation and prediction of transport properties*. PhD Dissertation, University of California at Berkeley, 2006.
- [28] Qisu Zou, Shuling Hou, Shiyi Chen, and Gary D. Doolen. An improved incompressible lattice Boltzmann model for time-independent flows. *Journal of Statistical Physics*, 81(1/2):35–48, 1995.
- [29] Qisu Zou and Xiaoyi He. On pressure and velocity boundary conditions for the lattice Boltzmann BGK model. *Physics of Fluids*, 9(6):1591–1598, 1997.
- [30] A. Revil and P. W. J. Glover. Theory of ionic-surface electrical conduction in porous media. *Physical Review B*, 55(3):1757–1773, 1997.
- [31] Dmitriy B. Silin, Guodong Jin, and Tad W. Patzek. Robust determination of the pore space morphology in sedimentary rocks. In *SPE Annual Technical Conference and Exhibition Meeting*, Denver, Colorado, USA, 2003.
- [32] Dmitriy B. Silin, Guodong Jin, and Tad W. Patzek. Robust determination of the pore-space morphology in sedimentary rocks. *Journal of Petroleum Technology*, 56(5):69–70, 2004.
- [33] L. M. Schwartz, F. Auzerais, J. Dunsmuir, N. Martys, D. P. Bentz, and S. Torquato. Transport and diffusion in three-dimensional composite media. *Physica A*, 207(1-3):28–36, 1994.
- [34] L. L. Latour, R. L. Kleinberg, P. P. Mitra, and C. H. Sotak. Pore-size distribution and tortuosity in heterogeneous porous media. *Journal of magnetic Resonance, Series A*, 112(1):83–91, 1995.
- [35] Lawrence M. Schwartz, Edward J. Garboczi, and Dale P. Bentz. Interfacial transport in porous material: Application to dc electrical conductivity of mortars. *J. Appl. Phys.*, 78(10):5898–5908, 1995.
- [36] Michael D. Wilson and Edward D. Pittman. Authigenic clays in sandstones: recognition and influence on reservoir properties and paleoenvironmental analysis. *Journal of Sedimentary Petrology*, 47(1):3–31, 1977.
- [37] John W. Neasham. The morphology of dispersed clay in sandstone reservoirs and its effect on sandstone shaliness, pore space and fluid flow properties. In *SPE Annual Technical Conference and Exhibition*, 1977.
- [38] C. A. Cade, I. J. Evans, and S. L. Bryant. Analysis of permeability controls: a new approach. *Clay Minerals*, 29:491–501, 1994.

-
- [39] K. M. Diederix. Anomalous relationships between resistivity index and water saturation in the Rotliegend sandstone (The Netherlands). In *SPWLA 23rd Annual Logging Symposium*, 1982.
- [40] M. H. Waxman and L. J. M. Smits. Electrical conductivities in oil-bearing shaly sands. *SPE Journal*, 8:107–122, 1968.
- [41] Martin J. Blunt, Matthew D. Jackson, Mohammad Piri, and Per H. Valvatne. Detailed physics, predictive capabilities and macroscopic consequences for pore-network models of multiphase flow. *Advances in Water Resources*, 25(8-12):1069–1089, 2002.
- [42] G. E. Archie. The electrical resistivity log as an aid in determining some reservoir characteristics. *Trans. AIME*, 146:54–62, 1942.
- [43] M. H. Waxman and E. C. Thomas. Electrical conductivities in oil-bearing shaly sands: I. The relation between hydrocarbon saturation and resistivity index. II. The temperature coefficient of electrical conductivity. *Society of Petroleum Engineers Journal*, 14:213–225, 1974.
- [44] A. E. Bussian. Electrical conductance in a porous medium. *Geophysics*, 48(9):1258–1268, 1983.
- [45] C. Clavier, G. Coates, and J. Dumanoir. Theoretical and experimental bases for the dual-water model for interpretation of shaly sands. *Society of Petroleum Engineers Journal*, 24(2):153–168, 1984.
- [46] Steve Taylor and Ron Barker. Resistivity of partially saturated Triassic sandstone. *Geophysical Prospecting*, 50(6):603–613, 2002.
- [47] David Linton Johnson, Joel Koplik, and Lawrence M. Schwartz. New pore-size parameter characterizing transport in porous media. *Physical Review Letters*, 57(20):2564–2567, 1986.
- [48] Olivar A. L. de Lima and Mukul M. Sharma. A grain conductivity approach to shaly sandstones. *Geophysics*, 55(10):1347–1356, 1990.
- [49] R. D. Hazlett. Simulation of capillary-dominated displacements in microtomographic images of reservoir rocks. *Transport in Porous Media*, 20:21–35, 1995.
- [50] Markus Hilpert and Cass T. Miller. Pore-morphology-based simulation of drainage in totally wetting porous media. *Advances in Water Resources*, 24(3/4):243–255, 2001.